Advanced Steel Construction – Vol. 19 No. 4 (2023) 353–365
DOI:10.18057/IJASC.2023.19.4.4

BEHAVIOURS OF STEEL-CONCRETE COMPOSITE BEAMS AT LOW TEMPERATURES: MATERIALS AND STRUCTURES

Jia-Bao Yan, Er-Cong Kang * and Jian Xie *

School of Civil Engineering / Key Laboratory of Coast Civil Structure Safety of Ministry of Education, Tianjin University, Tianjin 300350, China
** (Corresponding author: E-mail: kangercong2010@163.com; xiejian@tju.eud.cn)*

ABSTRACT

This paper reported the low-temperature ultimate strength behaviours of steel-concrete composite beams (SCCBs) from material to structure levels. Firstly, low-temperature mechanical properties of constructional materials in SCCBs, e.g., concrete, headed studs, and mild steel plate for I-beams, were experimentally studied. The studies on constructional materials showed that decreasing the temperature (*T*) from 20 to -80 ℃, the strength and ductility of headed studs and I-beam were generally increased; the decreasing *T* increased the strength, but reduced the ductility of concrete. Followed, the shear and tensile behaviours of headed studs in concrete at different *T* levels of 20~-80 ℃ were experimentally investigated. Test results showed that decreasing *T* from 20 to -80 ℃ increased the shear and tensile resistance of headed studs, but showed different effects on ductility. Four-point bending tests on three SCCBs were performed at *T* of 20, -30 and -60℃ to investigate the low-temperature ultimate strength behaviours. These tests showed that at low temperatures all SCCBs failed in flexure with crushing of top concrete slab and yielding of bottom I-beam. Decreasing *T* from 20 to -30 and -60℃ increased the ultimate strength of SCCBs by 10% and 24%, respectively. A series of prediction equations were proposed to incorporate the effects of the decreasing *T* on compressive and tensile strength of concrete, shear and tensile capacity of studs, and ultimate bending resistance of SCCBs. Their accuracies have been validated by these material and member tests.

ARTICLE HISTORY

Received: 22 February 2023
Revised: 22 May 2023
Accepted: 25 May 2023

KEYWORDS

Steel-concrete composite beam;
Low temperature;
Composite structure;
Arctic engineering;
Shear stud;
Material test

1. Introduction

Steel-concrete composite (SCC) structure, in terms of an upper concrete slab connected to an underneath steel beam/plate (usually I-beam, or box section), is a relatively new type of structure that has been extensively applied in engineering structures. The extensive applications of SCC structures (SCCSs) in civil engineering constructions include composite floors, composite beams, bridge girders, and ice-resistant walls for the Arctic platforms. More recently, the applications of cold-region SCC engineering constructions keep increasing, e.g., the SCC bridge in Canada [1, 2], the Lhasa River Bridge in Northern China [3], and the Arctic oil platforms [4, 5].

In cold regions, the cooling environment with varying low temperatures in different seasons brings challenges to engineering constructions. According to the reports by Stepanova [6], the lowest temperature near the Arctic Circle at Verkhoyansk Siberia was -72 ℃. Meanwhile, the lowest temperature in the record of Northern China could drop to -50 ℃ [7]. These low temperatures definitely affect the mechanical properties of structural materials, steel-concrete interfacial bonding, and behaviours of SCCSs. Previous experimental investigations [8-10] showed that dropping temperature from the ambient to sub-zero increased the strengths but reduced the ductility of mild steel; however, due to the increased content of Niccolum in steel, the Arctic low temperatures have marginal influences on the ductility of high-strength steels, e.g., S690 [11], Q690 and Q960 [12]. Amounts of research works also showed that the concrete exposed to sub-zero temperatures received increased compressive strengths with large variations [13-15]. Moreover, the influences of sub-zero temperatures on the improved concrete compressive strength are independent of mix proportions and curing conditions of concrete [13]. MacLean and Lloyd [16] proposed the stress-strain constitutive law for concrete at low temperatures. Regarding the steel-concrete interfacial bonding strength at low temperatures, Yan et al. [17] observed that decreasing the temperature from 30 to -80 ℃ increased the bond strength by more than 200%. Dalen [1] contributed to the low-temperature shear resistance of connectors in SCC beams (SCCBs). However, the low temperatures studied by Dalen [1] were limited to -10 and -20 ℃ which were still much higher than the severest low temperatures in cold regions. Low-temperature structural studies of reinforced concrete (RC) members have been reported on bridge columns [18-21], RC beams [22, 23], FRP reinforced RC beams [24-26], and FRP confined RC columns [27, 28]. These studies focused on the evaluation and retrofitting of aged cold-region infrastructures in Canada. However, they were mainly performed for RC structures. Long et al. [2] checked the fatigue behaviours of SCCBs at the low temperature of -29 ℃, which provided limited information on the SCCBs at even lower temperatures. More recently, Yan et al. [29-34] contributed to compression performances of steel tubes and composite columns with mild strength, high strength and stainless steel tubes. More extended studies on compression behaviours of SCC walls have also been reported in Ref. [35-37]. All these researches showed that the sub-zero temperatures significantly improved the compression behaviours of composite members, e.g., improved compression capacity and ductility. However, as the key structural elements in the composite bridges or other infrastructures, the studies on behaviours of SCCBs are still very limited. Their low-temperature behaviours have not been understood. Therefore, it is necessary to carry out researches on ultimate strength behaviours of SCCBs at Arctic low temperatures.

This paper performed a series of studies on low-temperature ultimate strength behaviours of SCCBs from the material, component, and structural levels. Firstly, the low-temperature mechanical properties of steels and concretes involved in SCCBs were studied. Followed, push-out and pull-out tests were performed to study the shear and tensile behaviours of headed studs used in SCCBs, respectively. Finally, four-point bending tests on SCCBs at low temperatures were carried out. Including the experimental studies, corresponding analytical models were also developed to estimate the low-temperature ultimate strength of SCCBs.

2. Components in SCCBs and research objectives

Fig. 1 illustrates the different components in a typical SCCB, i.e., I-beam, concrete slab, steel reinforcements, and headed studs. Exposed to sub-zero temperatures, the mechanical properties of concretes and steels in SCCBs at low temperatures required detailed investigations. Moreover, the low-temperature bonding strength at steel-concrete interface also determines the cross-sectional bending behaviour of SCCB as well as uplifting of concrete slabs from the underneath I-beam. The low-temperature bonding strength at steel-concrete interface mainly comprises shear strength of bonding connectors along the tangent direction of interacting interface and pull-out resistance of connectors normal to this interacting interface. Finally, four-point bending tests on SCCBs were carried out for investigations on their sub-zero ultimate strength behaviours. All these experimental studies provided detailed information on the low-temperature ultimate strength behaviour of SCCBs.

3. Low-temperature materials properties of concrete in SCCBs

3.1. Concretes

Grade C45 normal weight concrete (NWC) was selected for SCCB in this study, and its mix proportions are given in Table 1. To obtain its low-temperature mechanical properties at -80, -60, -30, and 20 ℃, three concrete cubes (width=100 mm) and three prisms (width × depth × height = 100 × 100 × 300 mm^3) at each *T* level were prepared for the compression tests whilst cubes with the same dimension were prepared for the splitting tension tests. All these cubes/prisms were standardly cured, and corresponding tests were carried out at 28 days after NWC casting.

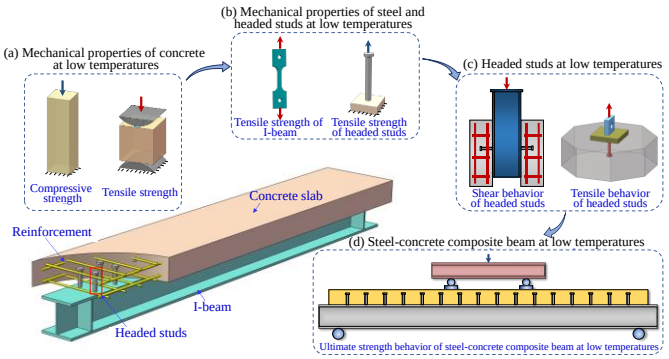

Fig. 1 Research objectives on steel-concrete composite beam at low temperatures

Table 1
Mix proportions of the normal weight concrete

Concrete grade	*w/c*	W_c (%)	Cement (kg/m^3)	Water (kg/m^3)	Fine aggregate (kg/m^3)	Coarse aggregate (kg/m^3)
C45	0.45	4.66	487	219	614	1080

w/c denotes water-to-cement ratio of NWC; W_c denotes moisture content of NWC.

3.2. Low-temperature uniaxial compressive behaviours of NWC

3.2.1. Test setup

Sub-zero compressive behaviours of NWC were obtained from compression tests on NWC prisms in a 500-ton testing machine. The setup of low-temperature compression tests on NWC prisms is given in Fig. 2. The NWC prism was firstly cooled down to the target temperature at a rate of 1 ℃/min in a cold storage and maintained at this temperature for at least 48 h. Then the prism was transferred to the 500-ton testing machine equipped with a cooling chamber. During the testing, a cooling chamber surrounding the prism with spraying liquid nitrogen gas (LNG) was adopted for the simulation of low-temperature environment. During the testing, one PT100 type of thermocouple, embedded in each prism during the casting, was used to measure the temperature of prism, and another four PT100 thermocouples were used for monitoring environmental temperatures of the chamber. All these readings of thermal couples assisted in controlling the testing temperatures for prisms within a tolerance of ±3 ℃. To obtain the recession branch of compressive sub-zero stress-strain (σ-ε) curves of NWC, displacement loading (0.2 mm/min) was used in this testing. Two LVDTs surrounding the prisms were adopted for the monitoring of their shortenings. The strain of each prism can be thus obtained through the shortening-to-height ratio of each test whilst the stress can be found from the measured reaction force over their sectional area.

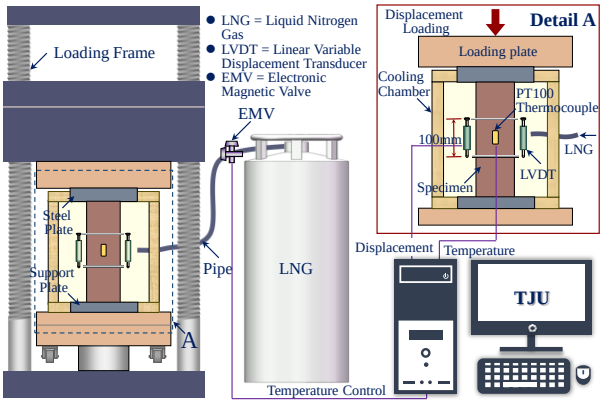

Fig. 2 Test setup of compressive tests on NWC prism at low temperatures

3.2.2. Sub-zero stress-strain curves of NWC

Fig. 3(a) plots the low-temperature stress-strain (σ-ε) curves of NWC. Fig. 3(b) plots the influences of T on cubic compressive strength (f_{cu}) and prism compressive strength of prisms (f_c) of NWC. They show that the sub-zero temperatures significantly influence the compressive σ-ε curves of NWC. As the sub-zero temperatures (T) decreases from 20 to -80 ℃, the compressive strength of NWC was increased; however, the ductility of NWC was slightly reduced. With T decreasing from 20 to -30, -60, and -80 ℃, the f_{cu} of C45 NWC was increased by 16.9%, 34.5%, and 43.7% respectively; the f_c of C45 NWC was increased by 28.1%, 64.0%, and 70.9%, respectively; meanwhile, the strain at f_c (i.e., ε_0) was increased by 35%, 15%, and 26%, respectively. These increments in compressive strength of NWC produced by the decreasing temperature are due to that the water in the pore of cement paste was frozen into ice, which increases the compactness of the NWC.

Based on the reported experimental σ-ε curves of NWC, the following empirical equations were developed to describe the sub-zero compressive σ-ε curves of NWC at low temperatures of -80 ~ 20 ℃;

$$\frac{\sigma}{f_c}=\frac{\beta(\varepsilon/\varepsilon_0)}{(\beta-1)+(\varepsilon/\varepsilon_0)^{\beta}} \tag{1}$$

$$\beta=\left(\frac{f_{cT}}{50.2}\right)^3+2.3 \tag{2}$$

where, σ and ε are stress and strain, respectively; f_{cT} is prism compressive strength of NWC at T, in MPa; β is shape parameter.

Fig. 3(a) compares these predicted low-temperature σ-ε curves of NWC with those experimental ones that exhibit reasonable estimations.

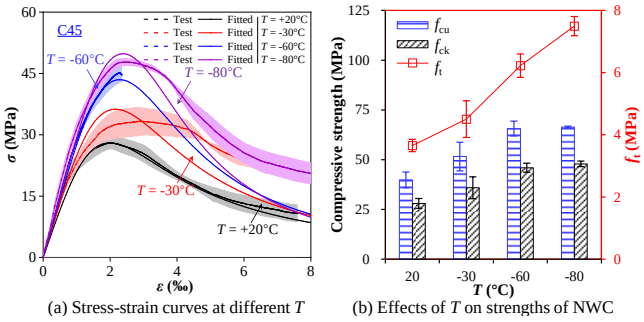

(a) Stress-strain curves at different T (b) Effects of T on strengths of NWC

Fig. 3 Effects of T on stress-strain curves and strengths of NWC

3.3. Low-temperature splitting tensile strength of NWC

The splitting tensile strengths (f_t) of NWC were obtained from the splitting tests on prisms following Chinese standard GB/T 50081 [38]. Twelve NWC cubes were prepared and tested at sub-zero temperatures of 20 to -30, -60, and -80 ℃. The test setup is similar to that used for compression tests in Fig. 2, and a cooling chamber infilled with the spraying LNG was also adopted for the cold-region environment. Table 2 lists these obtained tensile strengths of NWC at different T values. Fig. 3(b) depicts influences of T on f_t of NWC. It shows that with the decrease of T from 20 to -30, -60, and -80 ℃, the f_t of NWC receives average increments of 23%, 70%, and 105%, respectively.

Table 2
Material properties of normal weight concrete

Item	T (℃)	f_{cu} (MPa)	f_t (MPa)	f_{ck} (MPa)	ε_0 (με)	E_c (GPa)
CT+20-1	+20	39.4	3.44	29.1	2007	30.1
CT+20-2	+20	44.0	3.83	25.2	2014	25.0
CT+20-3	+20	36.2	3.69	29.8	1900	28.3
Mean		39.9	3.65	28.0	1974	27.8
COV		0.10	0.05	0.09		
CT-30-1	-30	59.6	4.76	36.8	2784	26.1
CT-30-2	-30	45.7	4.92	40.9	2351	32.9
CT-30-3	-30	49.6	3.83	30.0	2840	29.3
Mean		51.6/	4.50/	35.9	2658	29.4
COV		0.14	0.13	0.15		
CT-60-1	-60	63.9	6.62	43.4	2564	33.1
CT-60-2	-60	63.2	6.18	46.9	1965	28.7
CT-60-3	-60	69.9	5.87	47.6	2273	29.6
Mean		65.7	6.22	46.0	2267	30.5
COV		0.06	0.06	0.05		
CT-80-1	-80	66.9	7.17	49.5	2386	39.6
CT-80-2	-80	66.0	7.54	47.1	2491	35.4
CT-80-3	-80	66.4	7.78	47.1	2592	31.0
Mean		66.4	7.50	47.9	2490	35.3
COV		0.01	0.04	0.03		

T is temperature level; f_{cu} and f_{ck} are cubic and prism compressive strength; f_t is splitting tensile strength; ε_0 is peak strain; E_c is elastic modulus; COV is coefficient of variation.

4. Low-temperature mechanical properties of steel in SCCBs

4.1. Low-temperature mechanical properties of I-beam

Low-temperature mechanical properties of I-beam were obtained from tension tests according to GB/T 228.1-2010 [39] and GB/T 228.3-2019 [40]. Fig. 4(a) shows geometry of coupons cut from the I-beam. Nine coupons in total were prepared and they were tested at four temperatures of 20, -30, -60, and -80 °C. Table 3 provides the details of these testing parameters. Fig. 4(b) shows the tension test setup for these I-beam coupons. It shows that all the coupons were pin-connected to a set of holding rigid steel claps. Both the steel claps and coupon were surrounded by an insulation chamber that was used to maintain the low temperatures during the testing. LNG was also injected into the chamber to realize the low temperature of coupons. Once reached the target temperature, an additional 15 min were required to ensure the uniform distribution of the temperature of coupons. During the testing, two and four PT100 thermocouples were attached on the surfaces of coupons and chamber to measure the temperatures at different positions. The measured temperatures were used as the feedback for the inflowing rate of LNG to ensure that the coupons were maintained at the target temperature within a tolerance of ±3 °C. To instrument the strains of steel coupons, two linear strain gauges (LSGs) were installed on coupons as shown in Fig. 4(b). A low-temperature extensometer (gauging length = 50 mm) was also adopted to instrument the strains in coupons after yielding.

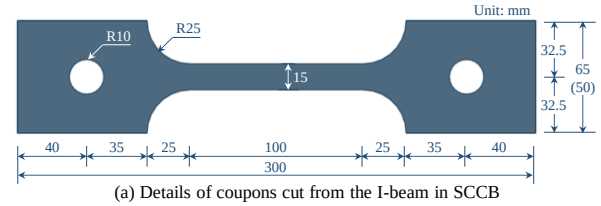

(a) Details of coupons cut from the I-beam in SCCB

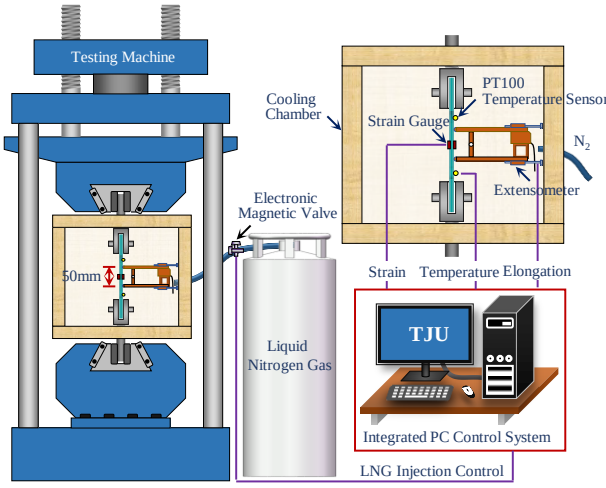

(b) Low-temperature tension tests on coupons cut from the I-beam in SCCB

Fig. 4 Tensile test setup on steel coupons cut from I-beam at low temperatures

Table 3
Details and tensile test results of I-beam

Item	T (°C)	ε_y (%)	ε_u (%)	ε_F (%)	ψ_s (%)	E_s (GPa)	f_y (MPa)	f_u (MPa)	I_{fy}	I_{fu}
BS+20-1	+20	0.1579	14.19	24.30	25.00	216.4	328.9	459.3	0.988	0.988
BS+20-2	+20	0.1530	16.48	26.08	25.62	224.2	336.6	470.6	1.012	1.012
BS-30-1	-30	0.1679	16.12	25.45	25.90	242.7	375.7	519.1	1.117	1.129
BS-30-2	-30	0.1637	15.95	26.36	24.84	226.5	379.1	535.2	1.151	1.139
BS-30-3	-30	0.1585	16.53	27.33	27.96	226.5	372.9	517.5	1.113	1.121
BS-60-1	-60	0.1840	15.18	25.48	25.02	234.0	417.3	564.2	1.214	1.254
BS-60-2	-60	0.1751	16.19	27.34	26.66	241.3	416.3	544.4	1.171	1.251
BS-80-1	-80	0.1980	19.49	30.46	30.98	233.0	424.7	554.1	1.192	1.276
BS-80-2	-80	0.1947	14.81	27.59	26.74	234.0	440.6	553.2	1.190	1.324

T is temperature level; E_s is elastic modulus; ε_y, ε_u, and ε_F are yield, ultimate, and fracture strain, respectively; ψ_s is percentage elongation after fracture; f_u and f_y are yield strength and ultimate strength, respectively; I_{fy} (or I_{fu}) equals yield (or ultimate) strength at T to its corresponding value at ambient temperature.

Fig. 5 plots the typical low-temperature σ-ε curves of I-beam. Table 3 lists the strength and ductility indexes of I-beam at low temperatures. They reflect that the low temperatures significantly improved the yield (f_y) and ultimate (f_u) strength of Q235 I-beam, and its ductility was slightly increased. Fig. 6 plots the effects of T on strength and ductility index of I-beam. It shows that; (1) The f_y, f_u, and elastic modulus (E_s) of I-beam increase with the decreasing T. With the decrease of T from 20 to -30, -60, and -80 °C, the f_y (or f_u) of I-beam is averagely improved by 13% (13%), 19% (25%), and 19% (30%), respectively; meanwhile, the E_s of I-beam is slightly increased by 5%, 8%, and 6%, respectively. These increments in strength and modulus of Q235 I-beam are due to that the decreasing T compacts the microstructure of I-beam and increases the molecular force. (2) The strain at ultimate strength (ε_u) and fracture strain (ε_F) increases with the decreasing T. With the decrease of T from 20 to -30, -60, and -80 °C, the ε_u (or ε_F) of I-beam is averagely improved by 6% (5%), 2% (5%), and 11% (15%), respectively.

Fig. 7 depicts the failure modes of steel coupons of I-beam after tested at different low temperatures. It shows that obvious necking took place in all the coupons tested at low temperatures. This further confirmed that ductile failure modes occurred to those I-beam steel coupons, which is consistent with the previous findings in Fig. 5 and 6.

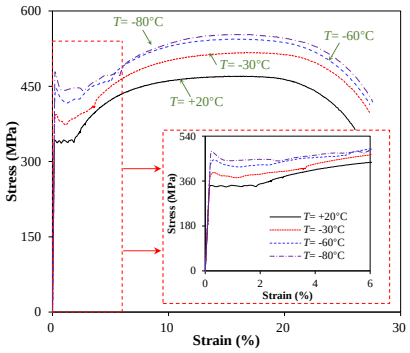

Fig. 5 Stress-strain curves of steel coupons cut from I-beam at low temperatures

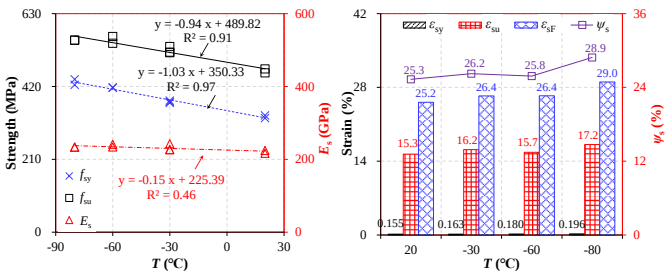

(a) Effect of T on strength and elastic modulus (b) Effect of T on ductility

Fig. 6 Effect of low temperatures on strength and ductility index of I-beam

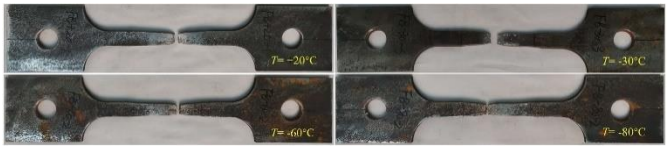

Fig. 7 Failure modes of steel coupons cut from I-beam at low temperatures

4.2. Low-temperature mechanical properties of headed studs [41]

Low-temperature mechanical properties of heads shear studs were obtained from direct tension tests using the setup in Fig. 8 [41]. Headed studs with d = 13, 16, and 19 mm were tested at low temperatures of -80, -60, -30, 0, and 20 °C, respectively. As shown in Fig. 8, the similar testing setup to the tension tests on steel coupons of I-beam was adopted. The cooling method to maintain the low temperature for tensile tests also adopted the same method as tension tests on I-beam. All the headed studs were firstly welded to a square steel plate (width × thickness=100 mm × 30 mm). After that, the top heads of stud and the bottom steel plate were installed to the holding frame connected to the testing machine. The cooling chamber surrounding this testing setup as shown in Fig. 8 was also used to realize the simulation of cooling environment. In addition, LNG was used as the cooling method for the tested specimens. Strain gauges and an extensometer were also to instrument elongations of the headed studs during the testing.

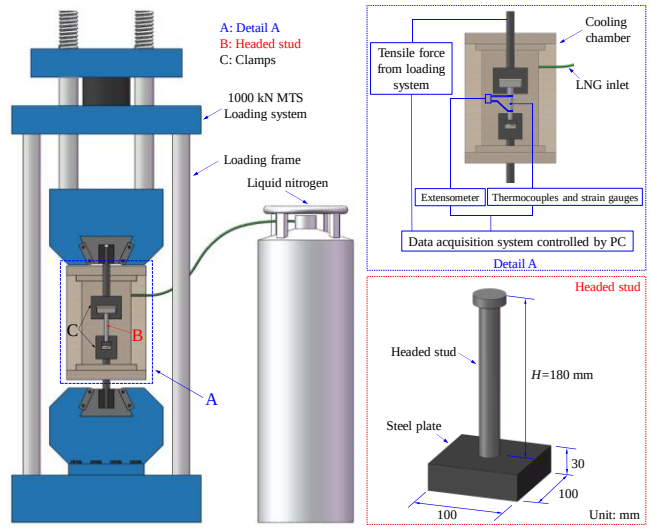

Fig. 8 Tensile test setup of headed studs at low temperatures [41]

Fig. 9 plots the low-temperature tensile σ-ε curves of headed studs. Table 4 provides the low-temperature mechanical properties of headed studs. They show that decreasing T significantly influences the tensile σ-ε curves of headed studs. Reducing T from 20 to -80 ℃ improves yield/ultimate strength and ductility of headed studs used in SCCBs. Fig. 10 depicts the influences of T on f_y, f_u, and E_s. It shows that with the reduction of T from 20 to 0, -30, -60, and -80 ℃, the f_y value of d=13 mm (or 16 mm, 19 mm) headed studs receives average increments of 2% (2%, 3%), 4% (4%, 7%), 8% (11%, 10%), and 19% (14%, 18%), respectively; the f_u value of d=13 mm (or 16 mm, 19 mm) headed studs is averagely increased by 3% (3%, 5%), 6% (7%, 9%), 12% (14%, 15%), and 20% (22%, 22%), respectively; meanwhile, the E_s value of d=13 mm (or 16 mm, 19 mm) headed studs receives slight average increase of 0% (0%, 3%), -2% (1%, 2%), 2% (2%, 3%), and 1% (2%, 2%), respectively. Moreover, Fig. 10 also reflects that the E_s value of headed studs exhibits low correlations with reducing T values, e.g., the correlation ratios (R^2) for d=13, 16, and 19 mm headed studs are only 0.07, 0.07, and 0.17, respectively. However, both the f_y and f_u values exhibit very high correlations with the decreasing T.

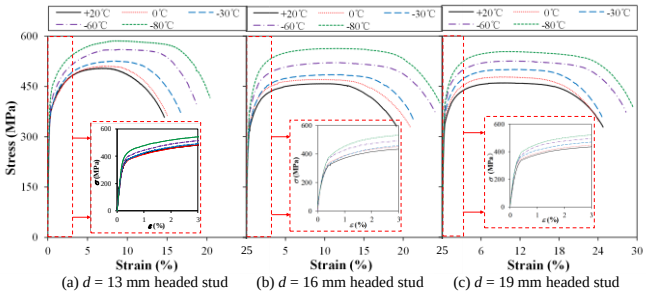

Fig. 9 Tensile stress-strain curves of headed studs at different low temperatures [41]

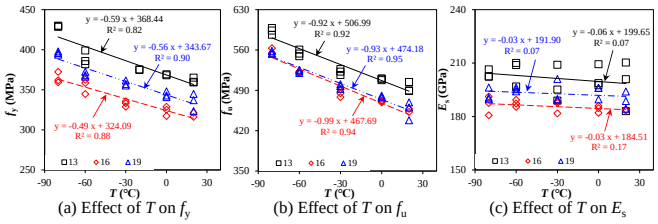

Fig. 10 Effect of low temperatures on tensile behavior of headed studs [41]

Based on the experimental results, Xie et al. [41] proposed empirical equations to estimate the influences of T on both f_y and f_u values of headed studs as follows;

$$f_{yT} = f_y e^{0.0012(T_0 - T)} \quad (3)$$

$$f_{uT} = f_u e^{0.0016(T_0 - T)} \quad (4)$$

where T is temperature, in °C, and -80 °C ≤ T ≤ 20 °C; f_{yT} and f_{uT} denote yield and ultimate strength at T, respectively.

Further validations proved that the proposed Eqns. (3) and (4) estimated reasonably the low-temperature yield and ultimate strength of headed studs [41].

Table 4
Details and tensile test results of headed studs

Item	T (°C)	d (mm)	ε_y (%)	ε_u (%)	ε_F (%)	ψ_{st} (%)	E_s (GPa)	f_y (MPa)	f_u (MPa)	I_{fy}	I_{fu}
HS1+20	+20	13	0.385	6.50	14.95	55.33	198.1	361.5	494.4	1.000	1.000
HS1+0	0	13	0.380	7.36	15.38	54.58	201.9	368.8	509.4	1.020	1.030
HS1-30	-30	13	0.391	7.80	16.22	54.07	197.7	375.1	522.1	1.038	1.056
HS1-60	-60	13	0.407	8.44	18.28	53.69	205.3	389.0	554.6	1.076	1.122
HS1-80	-80	13	0.408	8.60	19.81	53.54	203.8	429.3	592.8	1.188	1.199
HS2+20	20	16	0.378	10.06	20.20	57.64	183.7	318.8	455.3	1.000	1.000
HS2+0	0	16	0.379	9.36	21.28	56.97	184.2	323.7	470.7	1.015	1.034
HS2-30	-30	16	0.387	10.55	21.27	56.88	185.9	331.7	485.0	1.040	1.065
HS2-60	-60	16	0.392	11.72	24.42	56.53	187.3	355.2	521.3	1.114	1.145
HS2-80	-80	16	0.395	11.98	24.46	55.73	186.5	364.5	556.9	1.143	1.223
HS3+20	20	19	0.375	9.85	24.05	57.04	189.0	335.1	455.9	1.000	1.000
HS3+0	0	19	0.379	9.55	23.15	56.55	194.1	348.7	478.8	1.041	1.050
HS3-30	-30	19	0.381	10.57	24.42	56.32	193.4	358.1	496.9	1.069	1.090
HS3-60	-60	19	0.390	11.52	28.77	55.89	195.3	369.1	522.8	1.101	1.147
HS3-80	-80	19	0.404	11.81	29.06	55.90	192.2	395.8	555.3	1.181	1.218

T is temperature level; E_s is elastic modulus; ε_y, ε_u, and ε_F are yield, ultimate, and fracture strain, respectively; ψ_{st} is reduction ratio in cross-sectional; f_y and f_u are yield and ultimate strength, respectively; I_{fy} (or I_{fu}) equals yield (or ultimate) strength at T to its corresponding value at ambient temperature.

5. Low-temperature behaviours of headed studs in SCCBs

Behaviours of headed studs in SCCBs include concrete-steel interfacial shear behaviour and tensile behaviour in normal to the concrete-steel interface. The interfacial shear behaviour determines the cross-sectional bending resistance whilst the tensile behaviour of headed studs prevents the uplifting and separation of concrete slabs from the underneath I-beam.

5.1. Low-temperature shear behaviours of headed studs

5.1.1. Low-temperature push-out tests on headed studs

To investigate the shear behaviour of the basic component in SCCBs at low temperatures, e.g., headed studs, four groups of push-out tests were performed at four T levels of 20, -30, -60, and -80 °C. Fig. 11 shows the representative specimen prepared for tests. Each specimen comprises two concrete slabs connected to an I-beam using two headed studs for each concrete slab. The depth, width, and height of the concrete slab are 120, 300, and 350 mm, respectively. The Q235 HW150×150×10×7 mm^4 mild steel I-beam was adopted for the testing specimens. φ8 mm HRB 400 mild steel reinforcements with f_y=400 MPa were selected for the vertical and horizontal reinforcement mesh in the concrete slabs. Their layout and geometric details are shown in Fig. 11. Table 5 provides details of these testing specimens.

Fig. 12 shows the setup for the low-temperature push-out tests of headed studs. Similar to those low-temperature compression tests on concrete prisms, all push-out test specimens were firstly frozen to the target T level and maintained for 48 hours following instructions in GB51081 [42]. Then, they were moved into the cooling chamber installed to a 300-ton testing machine as shown in Fig. 12. After that, LNG was inlet into the cooling chamber to maintain the studied T level within the range of ±3 °C during the loading. The temperatures inside the concrete slab and on the surfaces of concrete slab and I-beam were measured by thermocouples embedded in the slab and installed on the surface of specimens, respectively. After achieving the target T, displacement loading (rate = 0.3 mm/min) directly acted on the top surface of I-beam (see Fig. 12). The beam-slab interfacial slips were measured by four LVDTs that were installed in the front of or below the headed studs along the

loading directions. The forces at each loading increment were automatically instrumented by the testing machine.

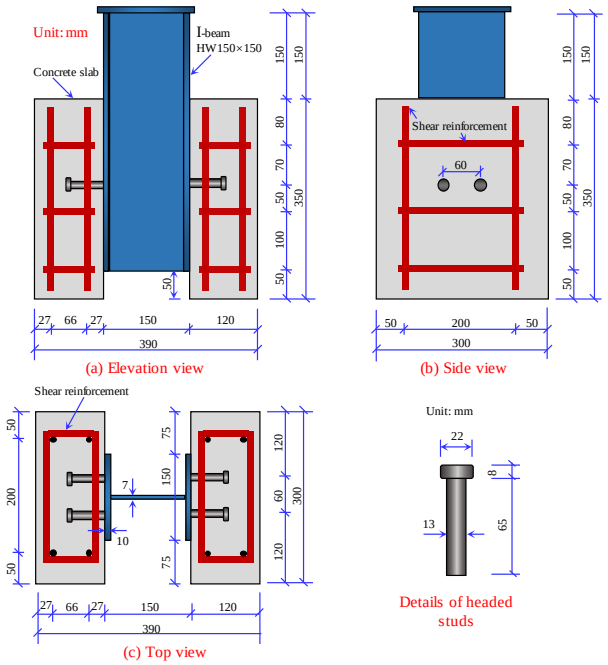

Fig. 11 Details of push-out specimens of headed studs

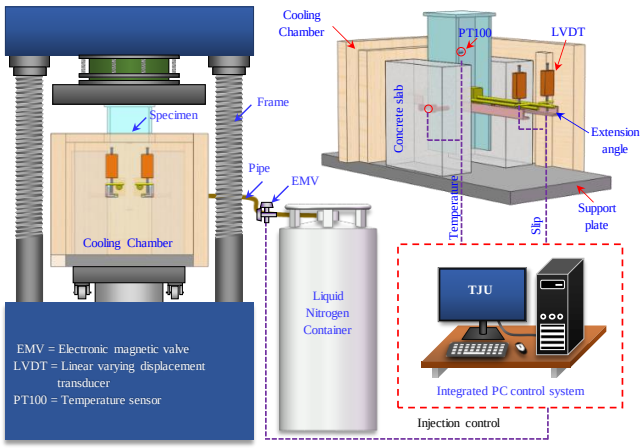

Fig. 12 Push-out test setup of headed studs at low temperatures

Table 5
Results of push-out tests of headed stud

Item	T (°C)	N_u (kN)	S_u (mm)	S_{max} (mm)	$K_{0.7Nu}$ (kN/mm)	$N_{u,P}$ (kN)	$\frac{N_u}{N_{u,P}}$	Failure mode
ST+20-1	+20	82.4	6.69	6.97	86.9	50.5	1.63	S+C
ST+20-2	+20	80.3	5.69	6.26	115.9	50.5	1.59	S+C
ST-30	-30	77.3	3.35	5.05	77.7	61.6	1.25	S+C
ST-60	-60	82.0	6.11	6.53	123.9	67.8	1.21	S+C
ST-80	-80	92.5	5.77	6.27	179.4	71.9	1.29	S
Mean							1.39	
COV							0.14	

T is temperature level; d and h are diameter and height of headed stud; N_u and $N_{u,P}$ are experimental and predicted ultimate shear resistance of headed stud, respectively; S_u and S_{max} are slip corresponding to N_u and $0.9N_u$ of the headed stud connectors; $K_{0.7Nu}$ is secant stiffness at $0.7N_u$; C and S are concrete splitting and stud fracture failure, respectively.

5.1.2. Failure modes

Fig. 13(a)-(d) plots the low-temperature failure modes of push-out specimen of headed studs. It shows that typical failure modes occurred to the push-out testing specimens are shear fracture of headed studs that occurred at their root positions, local crushing of NWC that took place near the root of studs, and cracks in the concrete slabs in specimens ST+20, ST-30, and ST-60. It also shows that cracks in the concrete slab were not observed in specimen ST-80 which was tested at -80 °C. This is because the decreasing T improves the compressive and tensile strengths of NWC that deterred the cracking of concrete slab. No differences in the failure modes exist among push-out specimens at 20, -30, and -60 °C.

Fig. 13 Failure modes of push-out specimens of headed studs at low temperatures

5.1.3. Shear-slip behaviours

Fig. 14 plots the typical low-temperature shear-slip (N-S) curves of a single headed stud. Fig. 15 reports the general low-temperature N-S curves for headed studs. They show that the low-temperature N-S curves of headed stud exhibit no obvious differences to the ambient one except the curve of ST-30. Their behaviours can be summarized as elastic, nonlinear, hardening, and recession stages. The threshold point between elastic and nonlinear stages locates at about 50~70% ultimate shear resistance (N_u). The nonlinearities of stage II are mainly produced by the yielding of headed studs and nonlinear behaviours of concrete slabs. After that, the strength hardening of the headed studs determines the behaviour of the third working stage. Finally, the N-S curves reached their peak shear resistance and the headed studs at one side of the I-beam were sheared off from the I-beam. Thus, the recession N-S curves exhibit sharp drops (shear fractures at one side of I-beam occurred to the two studs at the same time) or zigzag line (shear fractures of the two studs at one side of the I-beam did not occur at the same time).

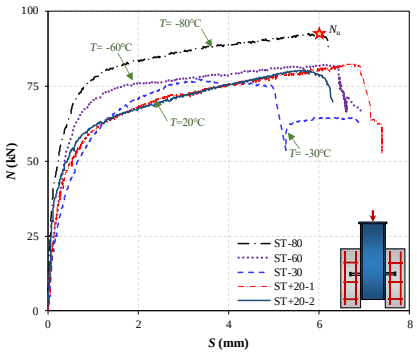

Fig. 14 Shear-slip curves of headed studs at different low temperatures

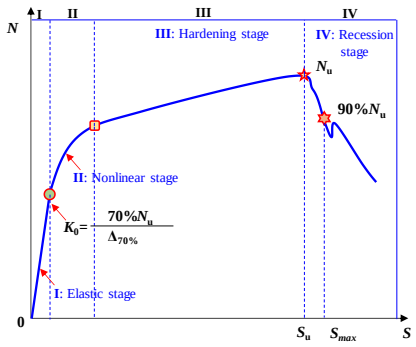

Fig. 15 General N-S curves of headed studs at low temperatures

5.1.4. Stiffness, strength and ductility

Determining the shear stiffness ($K_{0.7Nu}$) of N-S curves follows the method as shown in Fig. 15 [43], which equals 70% N_u to its corresponding slip, $\Delta_{70\%}$.

The N_u of headed studs can be obtained from their *N*-*S* curves. The ductility of these *N*-*S* curves of headed studs can be evaluated by the index of S_{max} at 90% N_u of recession *N*-*S* curves as illustrated in Fig. 15 [44]. Finally, these values are determined as listed in Table 5.

5.1.5. Discussions

Fig. 16 plots the influences of *T* on low-temperature strength, stiffness, and ductility of headed studs. It reveals that decreasing *T* from 20 to -80 °C generally increases the shear capacity, but slightly reduced the ductility of headed studs. With the decrease of *T* from 20 to -30, -60, and -80 °C, the N_u of studs was improved from 81.4 kN to 77.3, 82.0, and 92.5 kN with increments of -5%, 1%, and 14%, respectively ("-" value means decrease); meanwhile, the $K_{0.7Nu}$ of headed stud was increased from 101.4 kN/mm to 77.7, 123.9, and 179.4 kN with increments of -23%, 22%, and 77%, respectively ("-" value means decrease); however, the S_{max} of headed stud was reduced from 6.62 mm to 5.05, 6.53, and 6.27 mm corresponding to reductions of 24%, 1%, and 5%, respectively. The reason for these improvements in shear strength and stiffness is that the low temperatures improve the compressive strength of NWC and shear strength of headed studs. However, the decreasing *T* makes the frozen NWC more brittle which might cause the reduced slip capacity of headed studs.

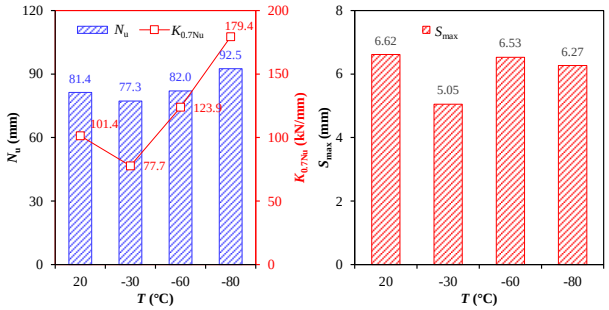

(a) Effect of *T* on strength and stiffness (b) Effect of *T* on slip capacity

Fig. 16 Effect of *T* on shear strength, stiffness, and slip capacity of headed studs

5.1.6. Prediction equations on shear resistance of headed studs at low temperatures

The prediction equations on low-temperature shear resistance of headed studs are proposed by the main authors [44] as the following;

$$N_{uT} = 0.43A_s\sqrt{f_{cT}E_{cT}} \le 5.8\kappa f_u A_s \left(\frac{E_{cT}}{E_{sT}}\right)^{0.41}\left(\frac{f_{cT}}{f_{uT}}\right)^{0.39} \quad (5)$$

$$\kappa = \begin{cases} 0.2(h/d+1) & \text{for } h/d \le 4.0 \\ 1 & \text{for } h/d > 4.0 \end{cases} \quad (6)$$

where, A_s denotes the stud's cross-sectional area, in mm^2; E_{cT} (or E_{sT}) denotes elastic modulus of concrete (or stud) at *T*, in MPa; f_{cT} denotes compressive strength of NWC at *T*, in MPa; f_{uT} denotes ultimate strength of stud at *T*, in MPa; *h* (or *d*) is the stud's height (or diameter), in mm.

Table 5 provides the theoretical predictions on low-temperature shear resistance of studs. It shows that the prediction equations provide conservative estimations on low-temperature shear resistances of studs. The average and COV for five predictions equal 1.39 and 0.14, respectively. Eqns. (5) and (6) could be used for the estimations on low-temperature shear resistance of headed studs.

5.2. Low-temperature pull-out behaviours of headed studs [45]

Low-temperature pull-out behaviours of studs embedded in the concrete slab resist the uplifting of concrete slab from the underneath I-beam in SCCBs. The tensile resistance of studs embedded in the concrete slab is obtained from the pull-out tests. The authors have performed the pull-out tests in Ref. [45] and herein summarize the relevant findings.

5.2.1. Low-temperature pull-out tests on headed studs

Fig. 17 illustrates the low-temperature pull-out tests on headed studs. There are totally eight specimens reported in Ref. [45] that were tested at four *T* levels of -80, -60, -30, and 20 °C with two specimens for every *T* level. Each specimen comprised one stud, a steel plate that the stud was welded to, an octagonal concrete slab, and a holding plate as shown in Fig. 18. Each headed stud was welded to a square 25 mm-thick steel plate, and it was cast in an octagonal concrete slab measuring 450×150 mm^2 in width × depth. A loading steel plate was welded to the square steel plate, and was pin-connected to the testing hydraulic jack as shown in Fig. 17. Before the pull-out testing, the specimens were reserved in a cold storage and maintained at the testing *T* level for 48 h following instructions in GB51081 [42]. After that, each specimen was moved into a chamber with insulation materials (see Fig. 17). A hydraulic jack was installed between the reaction frame and the concrete slab, and its loading end was connected to the pull-out specimen by the holding hole as shown in Fig. 17. After those installation procedures, this testing rig was sealed in the cooling chamber, and LNG was sprayed to keep the low temperatures. During this loading process, a PT100 thermocouple attached to the headed stud and four PT100 thermocouples installed in the cooling chamber were used to instrument temperatures inside and outside the pull-out testing specimens. After achieving the testing *T*, vertical tensile displacement (rate=0.5 mm/min) was applied to the headed studs. During this process, the vertical displacement/elongation (Δ) of the headed stud was measured by four LVDTs (see Fig. 17). The reaction force at each increment of Δ was instrumented by a load cell. In addition, during the whole process, the temperatures of the pull-out specimen should be controlled within ±3 °C. Table 6 provides more details of these pull-out test specimens.

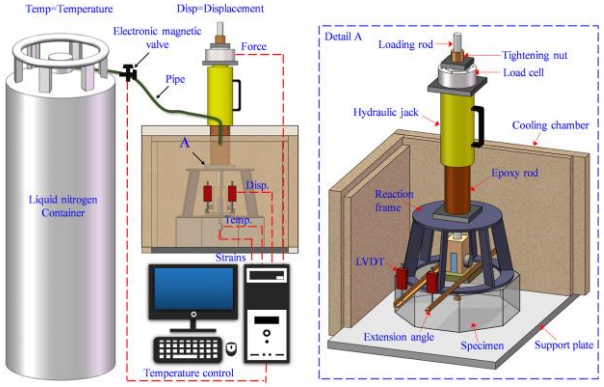

Fig. 17 Pull-out test setup of headed studs at low temperatures [45]

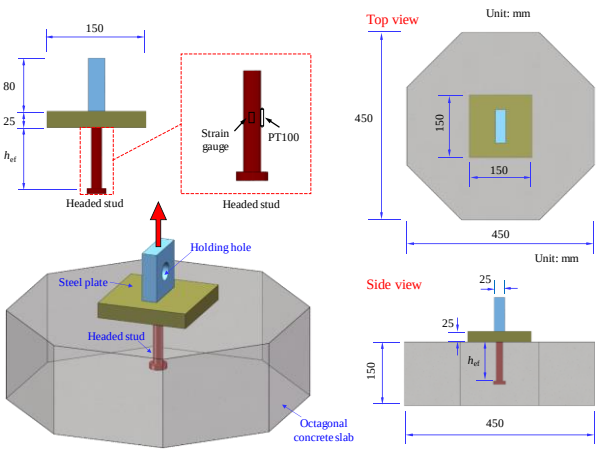

Fig. 18 Details of pull-out specimens of headed studs [45]

Table 6
Details and results of pull-out tests of headed studs

Item	*T* (°C)	h_{ef}/d	F_u (kN)	Δ_{Fu} (mm)	$K_{0.3Fu}$ (kN/mm)	$F_{u,P}$ (kN)	$\frac{F_u}{F_{u,P}}$	Failure mode
SF+20-1	+20	5.75	106.3	1.98	318.9	100.3	1.06	C + SP
SF+20-2	+20	5.75	103.8	1.61	283.1	100.3	1.04	SP
SF-30-1	-30	5.75	111.9	5.40	335.7	113.3	0.99	S
SF-30-2	-30	5.75	110.2	5.55	330.6	113.3	0.97	S
SF-60-1	-60	5.75	119.3	5.75	340.9	119.9	1.00	S
SF-60-2	-60	5.75	117.7	5.68	353.1	119.9	0.98	S
SF-80-1	-80	5.75	125.0	5.61	304.9	123.8	1.01	S
SF-80-2	-80	5.75	98.8	0.87	370.5	123.8	0.80	W
Mean							0.98	
COV							0.08	

T is temperature level; h_{ef} and d are effective embedment depth and diameter of a headed stud, respectively; h_{ef}/d is ratio of effective embedment depth of a headed stud to its diameter; F_u and Δ_{Fu} are ultimate pull-out resistance and corresponding displacement, respectively, of a headed stud in the test; $F_{u,P}$ is predicted ultimate pull-out resistance of a headed stud; $K_{0.3Fu}$ is secant stiffness at 30% of the ultimate load; C, SP, S, and W are concrete breakout, concrete splitting, steel fracture, and welding failure, respectively.

5.2.2. Failure modes

Fig. 19 shows the failure modes of pull-out specimens at low temperatures. For specimens tested at 20 °C, one specimen failed in concrete breakout failure with a characteristic of a pulled-out cone from the concrete specimen, and the other one failed in splitting of the concrete slabs due to insufficient splitting strength of NWC. For the rest pull-out testing specimens tested at -30, -60, and -80 °C, steel tensile fracture occurred to the headed studs except ST-80-1 which failed in the weld at the plate-stud connecting position. This clearly reveals that the low temperature deters the splitting or breakout failure of the concrete slab. This is because the low temperature increased the tensile strength of NWC which avoids the splitting or breakout failure of concrete slab.

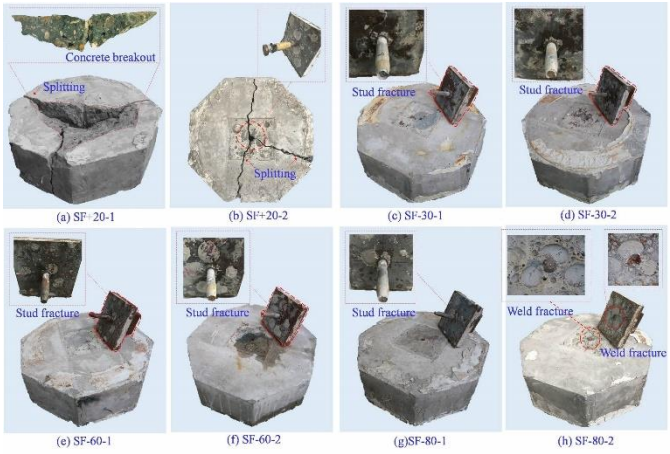

Fig. 19 Failure modes of pull-out test on headed studs at low temperatures [45]

5.2.3. Tension load-elongation (F-Δ) curves

Fig. 20 plots the average low-temperature F-Δ curves of headed studs, and Fig. 21 summarizes the general low-temperature F-Δ behaviours of studs under tension. They show that these F-Δ curves can be summarized into three patterns depending on their failure modes. For pull-out test specimens exhibiting steel fracture of headed stud, the F-Δ curves exhibit a ductile pattern with a linear, nonlinear, strength hardening, and recession branch, which is similar to the tensile mechanical behaviours of headed studs. The strength hardening branch is mainly determined by the strength hardening of material mechanical behaviours as shown in Fig. 9. For pull-out specimens exhibiting splitting failure mode in concrete slab or weld fracture of headed studs, the F-Δ curves exhibit a brittle behaviour with a linear, short nonlinear, and a sharp recession branch. The reason for the brittle manner without strength hardening development and a short nonlinear branch of F-Δ curves is due to that the resistance of the specimen at splitting failure of concrete slab is much smaller than its tensile fracture resistance of studs, which stops the strength hardening of studs. For the specimen failed in breakout of concrete slab mode, the F-Δ curves exhibit the most brittle behaviour with only linear and recession branch in its curves, which means the concrete breakout resistance of concrete slab is even smaller than the tensile yielding resistance of studs.

One interesting finding is that the low temperatures do not reduce the ductility of headed studs in concrete slabs under tension, and they generally improve the ductility of tensile F-Δ curves of headed studs. As the low temperatures go down beyond -30 °C, the F-Δ curves do not exhibit brittle mode any more. This is because the low temperatures increased the tensile and compressive strength of NWC much faster than those increments in tensile strength of raw stud materials, which means the much larger improved concrete breakout/splitting resistance of concrete slabs than the tensile strength of headed stud, e.g., as T reduces from 20 to -80 °C, the increments of concrete cubic compressive strength, concrete tensile strength, and yield/ultimate strength of studs equal to 44%, 105%, and 17%/20%, respectively.

5.2.4. Discussions

Fig. 22 shows the effects of T on ultimate pull-out resistance (F_u), initial stiffness ($K_{0.3Fu}$), and elongation at F_u (Δ_{Fu}). It shows that with the reduction of T from 20 to -30, -60, and -80°C, the average F_u of headed stud is improved from 105.1 kN to 111.1, 118.5, and 125.0 kN with increments of 6%, 13%, and 19%, respectively; meanwhile, the $K_{0.3Fu}$ of headed stud is averagely increased from 301.0 kN/mm to 333.2, 347.0, and 370.5 kN/mm with increments of 11%, 15%, and 23%, respectively; however, the Δ_{Fu} of headed stud is averagely improved from 1.80 to 5.48, 5.72, and 5.61 mm with increments of 204%, 218%, and 212%, respectively. These increments in pull-out capacity are mainly due to the increased strength and modulus of both NWC and headed studs. Moreover, with the same reduction of T, both tensile and compressive strengths of NWC exhibit much larger increments than those of headed studs, which guarantees the tensile fracture of headed studs occurred prior to the occurrence of breakout or splitting of the concrete slab. This also explains the improved ductility of headed studs. Moreover, as reported in section 4.2, the ductility of raw material of headed studs was not reduced and even slightly increased as the T reduces from 20 to -80 °C.

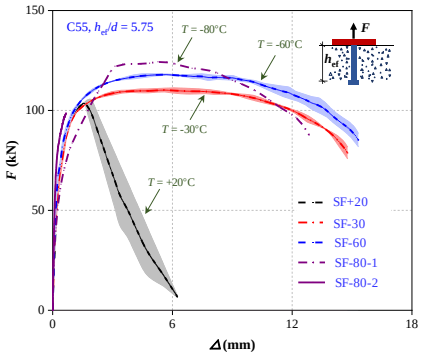

Fig. 20 Experimental F-Δ curves of headed studs at low temperatures [45]

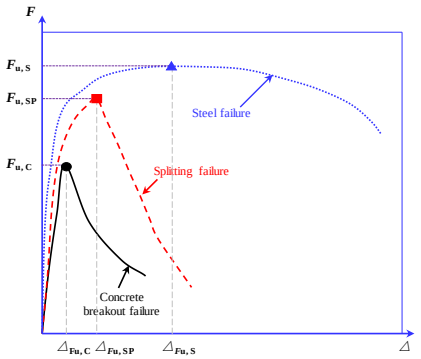

Fig. 21 General tension-elongation (F-Δ) curves of headed studs at low temperatures

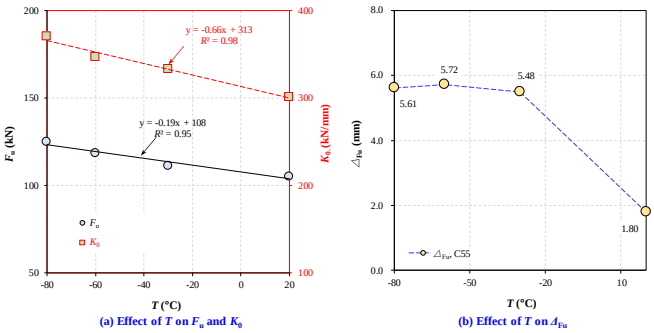

Fig. 22 Effect of T on tension strength, stiffness, and ductility of headed studs

5.2.5. Prediction equations on low-temperature pull-out resistance of headed studs

The low-temperature pull-out resistance of studs equals the smaller value of concrete breakout resistance (F_c) and tension resistance of headed studs (F_T) as the following;

$$F_{C,P} = \min\{F_C, F_T\} \tag{7}$$

$$F_C = k_{nc}\sqrt{f'_{c,T}}\,h_{ef}^{1.5} \tag{8}$$

$$F_T = A_s f_{uT} \quad (9)$$

where, $f'_{c,T}$ denotes cylinder compressive strength of NWC at T, in MPa; h_{ef} is the effective height of stud, in mm; A_s denotes the stud's cross-sectional area, in mm^2; f_{uT} denotes ultimate tensile strength of headed stud, in MPa.

Table 6 compares the predicted with those experimental low-temperature pull-out resistances of headed studs. It reflects that Eqns. (7)-(9) overestimates the pull-out resistance of stud by 2% with a COV of 0.08 for eight tests. This also proves the reasonable estimations of developed theoretical models on low-temperature pull-out resistance.

6. Ultimate strength behaviours of steel-concrete composite beams (SCCBs) at low temperatures

6.1. Four-point bending tests on SCCBs at low temperatures

6.1.1. Specimens

To investigate the low-temperature ultimate strength behaviours of SCCBs, three SCCBs, namely SCB+20, SCB-30, SCB-60, were prepared as shown in Fig. 23. Each SCCB comprises a top NWC slab, a bottom I-beam, headed studs at the slab-beam interface, and reinforcement mesh in the concrete slab. The Q235 mild steel HW125×125×6×9 mm^4 was used for the I-beam, and its mechanical properties at different low temperatures were tested and reported in section 4.1. The length of I-beam equals 1800 mm with stiffeners welded at the positions 100 mm off its both ends, where are the positions of the supports. The top NWC slab equals 1700, 300, and 85 mm in length, width, and depth, respectively. Headed studs (d=16 mm, height= 65 mm) are used for the fabrication of SCCBs. C45 NWC was used for the fabrication of NWC slab, and Table 7 lists its mechanical properties. φ8 and φ6 mm HRB 400 steel reinforcements (f_y=400 MPa) were used for reinforcement mesh in the NWC slabs as plotted in Fig. 23 (b). The main studied parameter is the low-temperature levels. Specimens SCB+20, SCB-30, SCB-60 were tested at 20, -30, and -60°C, respectively.

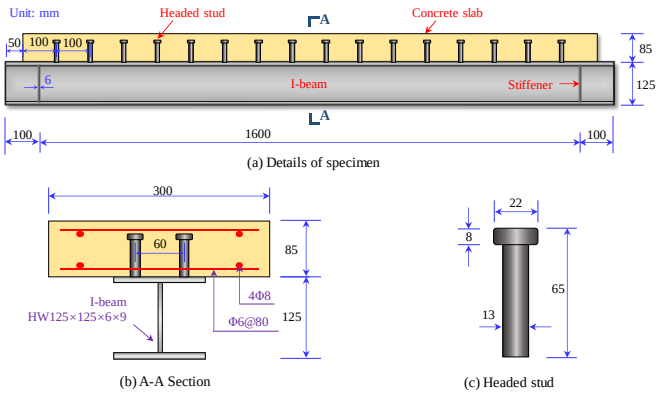

Fig. 23 Details of SCCBs for four-point bending tests at low temperatures

Table 7
Test results of steel-concrete composite beams

Item	T (°C)	f_c (MPa)	f_{sy} (MPa)	δ_y (mm)	δ_u (mm)	δ_{max} (mm)	K_0 (kN/mm)	P_y (kN)	P_u (kN)	$P_{u,E}$ (kN)	$\frac{P_u}{P_{uE}}$	P_{max} (kN)
SCB+20	+20	28.0	332.8	5.61	21.10	23.88	38.66	218.4	321.9	316.9	1.07	273.6
SCB-30	-30	38.8	375.9	4.69	20.84	31.85	40.83	186.0	355.0	368.0	1.02	301.8
SCB-60	-60	46.0	416.8	5.13	22.68	29.63	44.80	224.1	398.3	410.4	1.02	338.6
Mean											1.04	
COV											0.03	

T is temperature level; P_y denotes yield load in tests; P_u denotes ultimate load in tests; P_{max} denotes 85% of P_u; $P_{u,E}$ denotes predicted ultimate load; δ_y, δ_u, and δ_{max} denote the deflection of SCCB corresponding to P_y, P_u, and P_{max}; K_0 denotes secant stiffness of SCCB.

6.1.2. Setup and instrumentation

Fig. 24 plots the setup for the four-point bending tests on SCCBs. Before the testing, each SCCB was stored in the cold storage to maintain the target low temperature for 48 hours accordingly to GB51081 [42]. Then, the SCCB was moved to the loading machine equipped by a cooling chamber as shown in Fig. 24. The cooling chamber surrounded the SCCB with insulation materials and prevented the heat loss of specimens. Moreover, LNG was sprayed to SCCBs through openings in the top surface of chamber as shown in Fig. 24. During this process, two PT100 thermocouples were installed in the concrete slabs, and another four PT100 thermocouples attached to the surfaces of NWC slab and I-beam were used to measure the temperatures of specimens (see Fig. 24). These measurements of temperatures assisted the inflow control of the injecting LNG into the cooling chamber to ensure that the SCCBs remained within the target temperature range of ±3 °C.

Each specimen was installed to the rigid base on two round supports at both ends, which simulates the pin-pin boundary condition. The span of these two supports equals 1600 mm. Vertical loading in the displacement mode was transferred from the testing machine to the SCCB by a spreading I-beam. These two loading points locate 200 mm away from the mid-span (see Fig. 25). Three LVDTs were installed under the I-beam at mid-span and ±200 mm off mid-span to instrument deflections of SCCBs (see Fig. 25). To measure the steel-concrete interfacial slips, another four LVDTs were also installed along I-beam-slab interface at distances of 0, 200, 400, and 600 mm away from the mid-span as illustrated in Fig. 25. In addition, two more LVDTs were adopted at both ends of SCCB to record the slips between the concrete slab and I-beam. To measure strains along heights of the mid-span cross section, LSGs were installed as shown in Fig. 26.

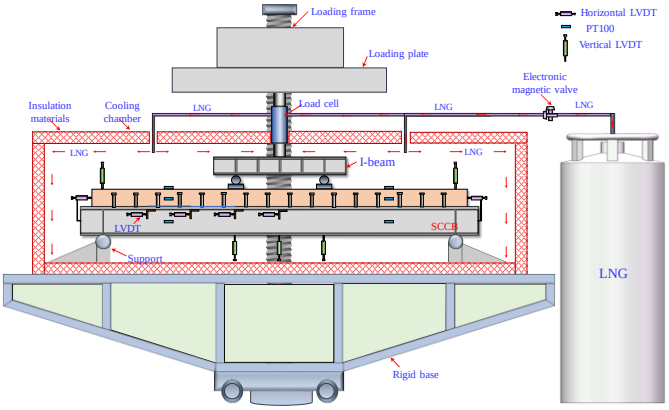

Fig. 24 Four-point bending test setup of SCCBs at low temperatures

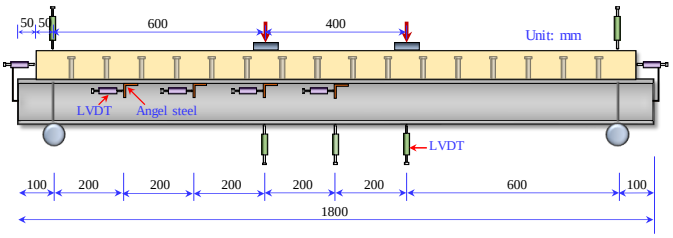

Fig. 25 Layout of LVDTs used in the bending tests on SCCBs

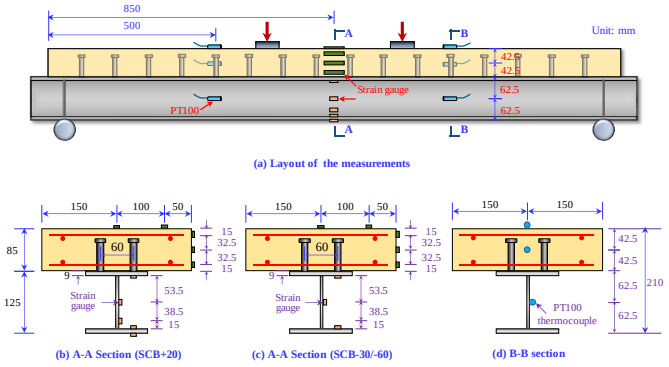

Fig. 26 Layout of strain gauges and thermocouples used in the bending tests on SCCBs

6.2. Failure modes

Figs. 27-29 plot the typical failure modes of SCCBs subjected to low-temperature four-point bending. They reflect that under sagging bending moment, concrete crushing occurred to the mid-span top flange of NWC slab. The depth of the crushed top flange of NWC slab equals about its 0.5 times depth. All the I-beams exhibited excessive deformation without occurrence of local buckling in their web or flange.

6.3. Load-deflection behaviours

The load-deflection (P-δ) curves of SCB+20, SCB-30, and SCB-60 are given in Fig. 30(a)-(c). These curves show that the P-δ curves of SCCBs exhibit a ductile manner with four stages of elastic, nonlinear developing, strength hardening, and recession stages. As the loading process, the curve of initial elastic stage (OA) ends as the bottom flange of I-beam starts to yield. Then, in stage II, the P-δ curves of SCCBs show a parabolic behaviour due to nonlinearities of I-beam and concrete. In the followed stage III, the SCCB exhibits hardening manner due to the strength hardening of I-beam, and the increasing rate of resistance slows down. Finally, the SCCBs achieve their peak resistances at the end of stage III. At the peak resistance, concrete crushing took place at the mid-span where suffered the maximum bending moment. The final recession stage exhibits decreased load carrying capacity.

Fig. 30 (d) compares the P-δ curves of SCCB tested at different T levels. Fig. 31 plots the influences of T levels on elastic stiffness (K_0), ultimate resistance (P_u), central deflection at P_u (δ_u), and ultimate deflection capacity (δ_{max}, the deflection at 85% P_u in recession P-δ curves). These curves show that the decreasing T slightly increased the elastic stiffness, but significantly increased the ultimate resistance of SCCBs. Moreover, the slope of strength hardening P-δ curves at low temperatures is larger than that at ambient temperatures. In addition, the ductility of SCCB was not reduced as the T level goes down from 20 to -60 ℃. As T decreases from 20 to -30, and -60℃, the P_u of SCCB is increased from 321.9 kN to 355.0 and 398.3 kN with increments of 10% and 24%, respectively; meanwhile, the K_0 of SCCB is increased from 38.7 kN/mm to 40.8 and 44.8 kN/mm with increments of 5% and 16%, respectively; however, the δ_u (or δ_{max}) of SCCB is increased from 21.1 (23.9) mm to 20.8 (31.9) and 22.7 (29.6) mm with increments of -1% (33%) and 8% (24%), respectively. This is because the decreasing T improves the compressive strength of NWC and yield strength of I-beam which explains the improved P_u of SCCB. Moreover, the low temperature also increases the elastic modulus of NWC and I-beam. As pointed in section 3 and 4, as the T reduces from 20 to -30 and -60 ℃, the E_{cT} of NWC is improved by 16% and 12%, respectively. However, sections 3 and 4 also show that the decreasing T did not reduce the ductility of headed studs and I-beam, which makes sure the marginal influences on the ductility of SCCBs.

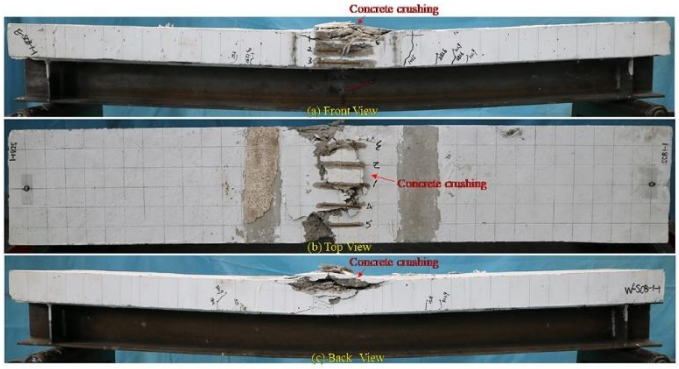

Fig. 27 Failure mode of SCB+20

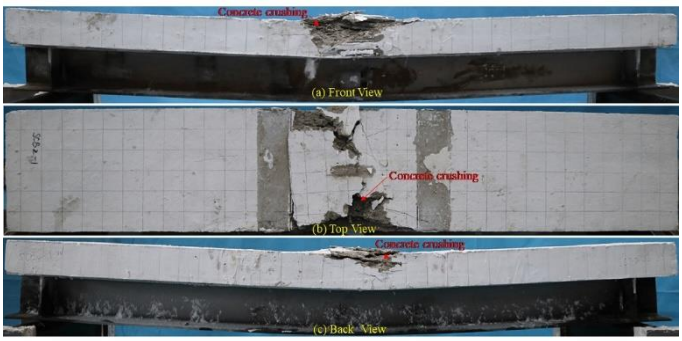

Fig. 28 Failure mode of SCB-30

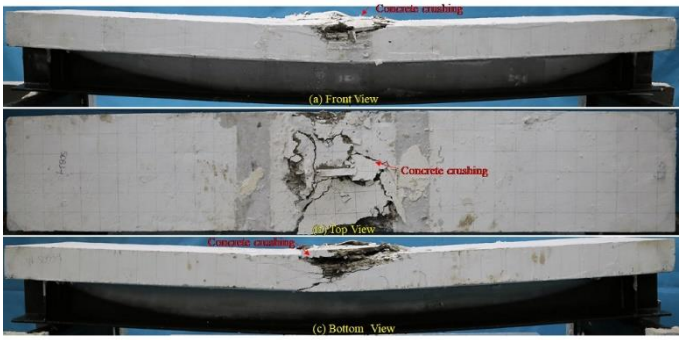

Fig. 29 Failure mode of SCB-60

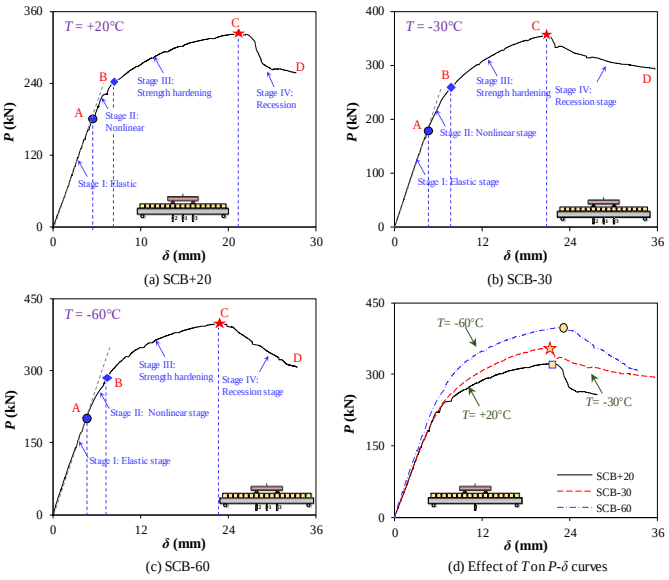

Fig. 30 Load-deflection curves of SCCBs under low-temperature four-point bending

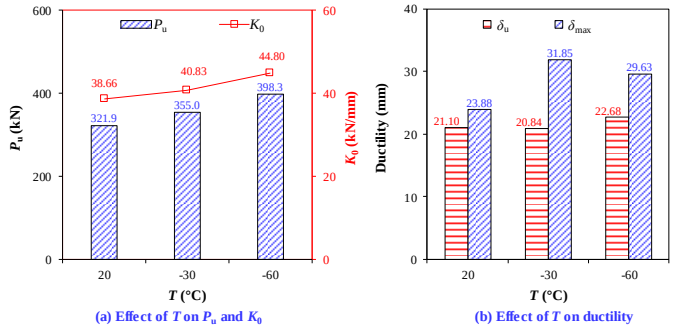

Fig. 31 Effect of T on strength and ductility index of SCCBs

6.4. Load-strain behaviours

Fig. 32 depicts the load-strain curves of mid-span cross-section as marked in Fig. 26. It shows that load-strain curves exhibit the same four-stage behaviour as those P-δ curves of SCCBs. It further confirms that the nonlinearities of load-strain (or P-δ curves) at the second working stage initiate as the bottom tip of I-beam yields. Thus, after stage II, strength hardening starts and the SCCBs achieved their P_u values whilst the top tip of NWC slab achieved their ultimate compressive strains of about 3000~5000με.

Fig. 33 depicts the mid-span strain versus height profiles at different loading levels. It reveals that as the reaction force of the SCCB is smaller than $0.9P_u$ the strain profiles are almost in a linear relationship with the height; as the reaction force of the SCCB is beyond $0.9P_u$ until P_u the linear strain distribution principle almost works even though there are some slight interfacial slips occurred. These observations confirm that the assumption of plane section still works for the SCCBs subjected to low-temperature bending since they were designed as the full-composite action.

6.5. Load-slip behaviours

Fig. 34 depicts the load-slip curves at different positions along SCCBs. It shows that these load-slip curves exhibit a similar four-stage manner to those P-δ (or strain) curves. At working stages I and II, the slips are almost in a linear relationship with the applied load, and the slips are smaller than 0.2 mm. The slips start to increase fast in the strength hardening stage and the maximum slip is about 1.0 mm which occurs at the locations of 400 ~ 600 mm away from the mid-span. Fig. 35 plots the slip profiles of different measured locations at different loading levels. It shows that (1) the slip starts to increase fast as the applied load is beyond 0.7P_u; (2) at the same loading level, the slips firstly increase and then decrease as the distance away from the mid-span increases, and the maximum slips occurred to the cross section locating 400 mm and 600 mm away from the mid-span for SCCB tested at ambient and low temperatures, respectively. This may be explained by the bending moment distribution and inner layout of the headed studs in the SCCBs.

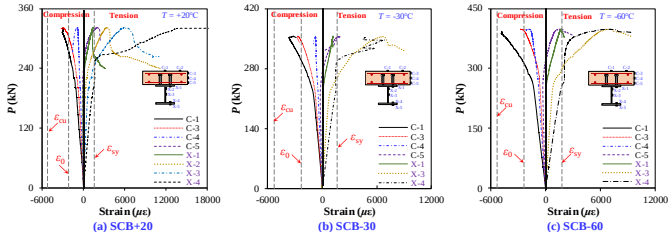

Fig. 32 Load-strain curves of concrete slab and I-beam at mid-span cross section

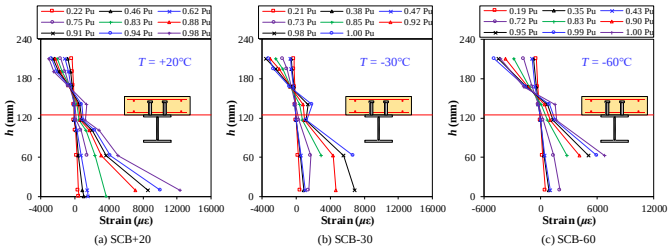

Fig. 33 Strain distribution profile along the height of the mid-span cross section at different loadings

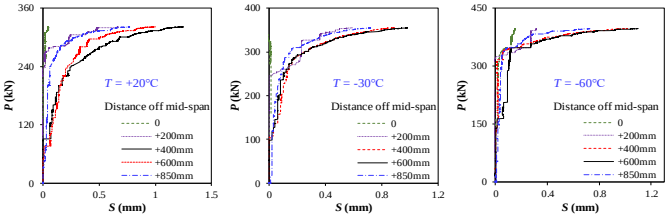

Fig. 34 Load-slip curves of SCCBs at different temperatures

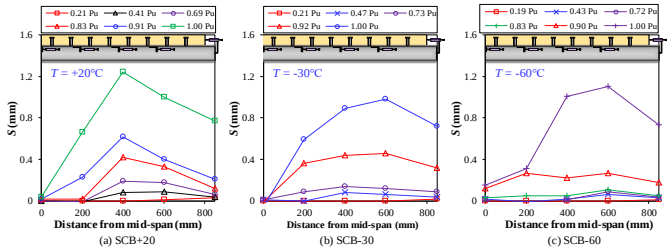

Fig. 35 Slip distribution file along the length of SCCBs at different loadings

6.6. Analysis on ultimate resistance of SCCB at low temperatures

Since the SCCBs failed in flexure, the bending resistance of SCCB at low temperatures (M_{uT}) can be obtained based on the following assumptions;

(1) Plane section remains plane (this has been checked in section 6.4); (2) Ignoring the NWC low-temperature tensile strength; (3) The I-beam achieves its yielding strength in both tension and compression zones.

Suffering sagging moment, the neutral axis may locate at different heights of the cross section, e.g., in the NWC slab, in the flange or web of I-beam. Therefore, the bending resistance of SCCBs at low temperatures can be found by assuming different positions of the neutral axis.

Case 1: Neutral axis in the NWC slab ($x<h_c$)

Fig. 36(a) plots the stress and internal force distribution diagram of the cross section at P_u as $x<h_c$. The low-temperature bending resistance of the SCCB can be found by finding the neutral axis position, i.e., the resultant internal compression force of the cross section equals to the internal tension force as the following;

$$C_c = T_{s1} + T_{s2} + T_{s3} \tag{10}$$

$$C_c = 0.85 f_{cT}^{'} x b_e; T_{s1} = f_{yT} h_t b_f; T_{s2} = f_{yT} h_w t_w; T_{s3} = f_{yT} h_b b_f \tag{11}$$

where b_e and b_f denote width of concrete slab and steel flange, respectively; h_t, h_b and h_w denote height of steel top and bottom flange, and steel web, respectively; h_c denotes depth of concrete slab; t_w denotes web thickness; x denotes distance between the neutral axis and top tip of compression concrete slab; $f_{cT}^{'}$ denotes cylinder compressive strength of NWC at T; f_{yT} denotes yield strength of I-beam at T; C_c denotes internal resultant force of compression concrete; T_{s1}, T_{s2} and T_{s3} denote internal resultant tensile load of top flange, web and bottom flange of I-beam, respectively.

Thus, the x is determined as the following;

$$x = \frac{f_{yT}(h_t b_f + h_w t_w + h_b b_f)}{0.85 f_{cT}^{'} b_e} \tag{12}$$

The ultimate bending moment of SSCB at T, i.e., $M_{u,T}$, is determined by;

$$M_{u,T} = 0.85 f_{cT}^{'} x b_e \left(h_c + \frac{h_t + h_w + h_b - x}{2}\right) \tag{13}$$

Case 2: Neutral axis in the flange of I-beam [$h_c \le x \le (h_c + h_t)$]

Fig. 36(b) plots the stress distribution diagram of cross section at P_u as $h_c \le x \le (h_c + h_t)$. As the neutral axis lies in the I-beam flange, the x value is determined by the resultant internal force equalling zero, i.e.,

$$C_c + C_{s1} = T_{s1} + T_{s2} + T_{s3} \tag{14}$$

$$C_c = 0.85 f_{cT}^{'} h_c b_e; C_{s1} = f_{yT}(x - h_c) b_f \tag{15}$$

$$T_{s1} = f_{yT}(h_c + h_t - x) b_f; T_{s2} = f_{yT} h_w t_w; T_{s3} = f_{yT} h_b b_f \tag{16}$$

where, C_c and C_{s1} denote internal resultant compressive forces of concrete slab and top flange of I-beam, respectively; T_{s1}, T_{s2}, and T_{s3}, denote internal resultant tensile load of top flange, web, and bottom flange of I-beam, respectively.

Thus, the x value is solved by the following equation;

$$x = \frac{f_{yT}(2h_c b_f + h_t b_f + h_w t_w + h_b b_f) - 0.85 f_{cT}^{'} h_c b_e}{2 f_{yT} b_f} \tag{17}$$

The $M_{u,T}$ of SCCB at low temperatures can be determined as the following;

$$\begin{aligned} M_{u,T} = {} & 0.5 T_{s1}(h_c + h_t - x) + T_{s2}(0.5 h_w + h_c + h_t - x) \\ & + T_{s3}(0.5 h_b + h_w + h_c + h_t - x) + C_c(x - 0.5 h_c) + 0.5 C_{s1}(x - h_c) \end{aligned} \tag{18}$$

Case 3: Neutral axis in the web of I-beam [$x > (h_c + h_t)$]

Fig. 36(c) plots the stress distribution diagram of cross section at P_u as $x > (h_c + h_t)$. As the neutral axis lies in the I-beam web, the x value can be found as the following;

$$C_c + C_{s1} + C_{s2} = T_{s2} + T_{s3} \tag{19}$$

$$C_c = 0.85 f_{cT}^{'} h_c b_e; C_{s1} = f_{yT} h_t b_f; C_{s2} = f_{yT}(x - h_t - h_c) t_w \tag{20}$$

$$T_{s2} = f_{yT}(h_w + h_c + h_t - x) t_w; T_{s3} = f_{yT} h_b b_f \tag{21}$$

where, C_c, C_{s1}, and C_{s2} denote internal resultant compressive forces of concrete slab, I-beam top flange, and I-beam web, respectively; T_{s2} and T_{s3} denote internal resultant tensile loads of I-beam web and I-beam bottom flange, respectively.

Thus, the x is solved as the following;

$$x = \frac{f_{yT}(h_w t_w + 2h_c t_w + 2h_t t_w + h_b b_f - h_t b_f) - 0.85 f_{cT}^{'} h_c b_e}{2 f_{yT} t_w} \tag{22}$$

The $M_{u,T}$ of SCCB now becomes;

$$\begin{aligned} M_{u,T} = & 0.5 T_{s2}(h_c + h_t + h_w - x) + T_{s3}(0.5h_b + h_c + h_t + h_w - x) \\ & + C_c(x - 0.5h_c) + C_{s1}(x - h_c - 0.5h_t) + 0.5 C_{s2}(x - h_c - h_t) \end{aligned} \tag{23}$$

Thus, the low-temperature bending resistance of SCCB can be found by procedures in Fig. 37. In addition, one point needs to be clarified is that the SCCB should be designed as a full-composite beam using Eqn. (5) for low-temperature shear resistance of studs in SCCBs. Regarding the partial composite SCCB, further studies are still required.

The ultimate load ($P_{u,T}$) of the SCCB is determined as follows;

$$P_{u,T} = 2M_{u,T} / a \tag{24}$$

6.7. Validations

Table 7 lists the predicted $P_{u,T}$ by the developed theoretical models with test values. It shows that theoretical models underestimate the load capacity of SCCBs SCB+20, SCB-30, and SCB-60 by 7%, 2%, and 2%, respectively. The average discrepancy of theoretical predictions is less than 4% that confirms their accurate estimations on ultimate load capacities of SCCB at low temperatures. However, these theoretical models still require more extensive validations.

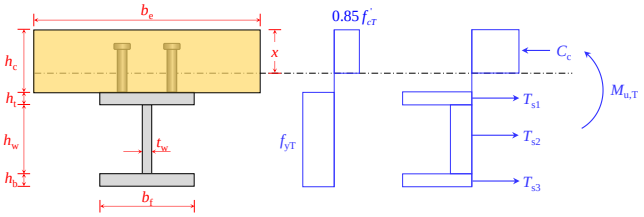

(a) Stress and internal force distribution diagram of the cross section as $x \le h_c$

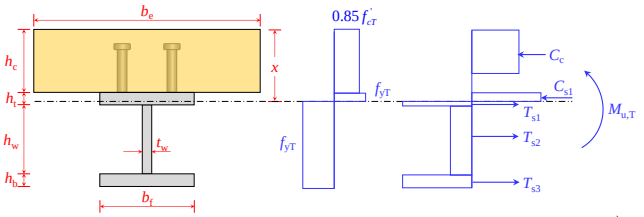

(b) Stress and internal force distribution diagram of the cross section as $h_c < x \le (h_c + h_t)$

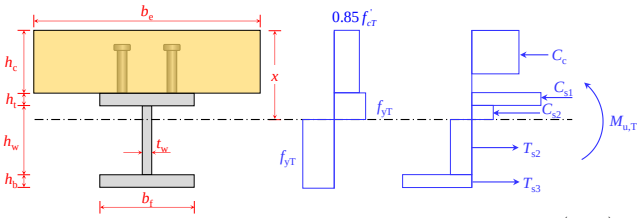

(c) Stress and internal force distribution diagram of the cross section as $x > (h_c + h_t)$

Fig. 36 Stress, stress and internal force distribution diagrams for SCCBs

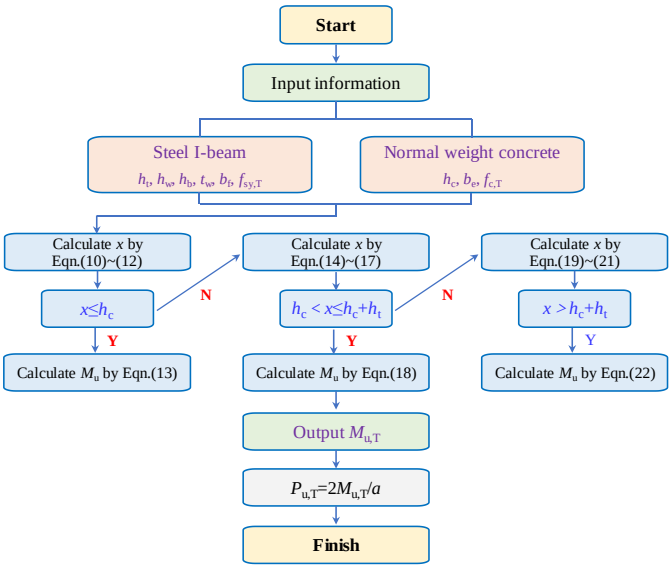

Fig. 37 Flow chart on determining low-temperature ultimate bending resistance of SCCBs

7. Conclusions

This paper reported a series of tests and analytical studies on behaviours of constructional materials in SCCBs and low-temperature ultimate strength behaviour of SCCBs. These studies on material and structural members support the following findings;

(1) With the decease of T from 20 to -30, -60, and -80 °C, the f_c of C45 NWC was increased by 28%, 64%, and 71%, respectively; meanwhile, the strain at f_c (i.e., ε_0) was increased by 35%, 15%, and 26%, respectively; the f_t of NWC receives average increments of 23%, 70%, and 105%, respectively. Eqn. (1)-(2) are developed to estimate the low-temperature stress-strain curves of NWC.

(2) The strength and modulus of mild steel Q235 for I-beam increases with the decreasing T, and its ductility was also improved with the decreasing T from 20 to -60°C. With the decrease of T from 20 to -30, -60, and -80 °C, the f_y (or f_u) of I-beam is averagely increased by 13% (13%), 19% (25%), and 19% (30%), respectively; meanwhile, the E_s of I-beam is slightly increased by 5%, 8%, and 6%, respectively; meanwhile, the average fracture strain of I-beam is improved by 5%, 5%, and 15%, respectively.

(3) The decreasing T slightly changed the modulus of headed studs within 3%. With the reduction of T from 20 to 0, -30, -60, and -80 °C, f_y of d=16 mm headed studs receives average increments of about 2%, 4%, 11%, and 14%, respectively; the f_u value of d=16 mm headed studs is averagely increased by 3%, 7%, 14%, and 22%, respectively. Eqns. (3) and (4) were developed to estimate the influences of T on f_y and f_u of headed studs.

(4) The typical failure modes of low-temperature push-out tests were shear fracture of headed studs at their roots, local crushing of NWC, and cracks in the concrete slabs. Reducing T from 20 to -80 °C generally improved the shear capacity, but slightly reduced the ductility of the headed studs. With the decrease of T from 20 to -80 °C, the N_u of headed stud was improved by 14%; however, the S_{max} of the headed stud was slightly reduced from 6.6 to 6.3 mm. Eqns. (5)-(6) were recommended to estimate the low-temperature N_u of headed studs.

(5) Low temperatures generally improved the pull-out ductility and resistance of headed studs. With the reduction of T from 20 to -80 °C, the F_u of headed stud is averagely increased by 19%; the ultimate elongation (Δ_{Fu}) of headed stud is averagely increased from 1.8 mm to 5.6 mm. Eqns. (7)-(9) were proposed for determining the low-temperature pull-out resistance of studs.

(6) The SCCBs subjected to low-temperature four-point bending exhibited flexural mode with concrete-slab crushing and yielding of bottom I-beam. The low temperature increased the ductility, elastic stiffness and ultimate resistance of SCCBs. As T decreased from 20 to -30, and -60°C, the P_u of SCCB was improved by 10% and 24%, respectively; the K_0 of SCCB was improved by 5% and 16%, respectively; the δ_u (or δ_{max}) of SCCB is increased by -1% (33%) and 8% (24%), respectively.

(7) The developed theoretical models, i.e., Eqns. (10)-(24) predicted reasonably the low-temperature ultimate bending resistance of SCCBs. The average discrepancy of three theoretical predictions on ultimate load capacities of SCCBs at low temperatures is less than 4%. However, these theoretical models still require more extensive validations.

Nomenclature

C_c Internal resultant compression force of concrete slab
C_{s1} Internal resultant compressive force of I-beam top flange
C_{s2} Internal resultant compressive force of I-beam web
E_c Modulus of elasticity of NWC
E_{cT} Modulus of elasticity of NWC at T
E_s Elastic modulus of steel
F_C Concrete breakout resistance of headed stud
F_T Tension resistance of headed stud
F_u Ultimate pull-out resistance of headed stud
$F_{u,P}$ Predicted ultimate pull-out resistance of headed stud
I_{fu} Ultimate strength at T to its corresponding value at ambient temperature of steel
I_{fy} Yield strength at T to its corresponding value at ambient temperature of steel
K_0 Initial stiffness of SCCB
$K_{0.3Fu}$ Secant stiffness at 30%F_u
$K_{0.7Nu}$ Secant stiffness at 70%N_u
$M_{u,T}$ Predicted ultimate bending moment of SCCB
N_u Ultimate shear resistance of headed stud
$N_{u,P}$ Predicted shear resistance of headed stud
P_{max} 0.85P_u of recession of P-δ curve of SCCB
P_u Ultimate resistance of SCCB
$P_{u,E}$ Predicted ultimate resistance of SCCB
P_y Yield load of SCCB
S_{max} Slip at 0.9N_u of recession of N-S curves
S_u Slip corresponding to N_u of headed stud
T Temperature level
T_{s1} Internal resultant tensile load of I-beam top flange
T_{s2} Internal resultant tensile load of I-beam web
T_{s3} Internal resultant tensile load of I-beam bottom flange
a Shear span of SCCB
b_e Width of concrete slab
b_f Width of I-beam flange
d Diameter of headed stud
f_c Prism compressive strength of NWC
f_{cu} Cubic compressive strength of NWC
f_{cT}' Cylinder compressive strength of NWC at T
f_c' Cylinder compressive strength of NWC
f_t Tensile strength of NWC
f_u Ultimate strength of steel
f_{uT} Ultimate strength of I-beam at T
f_y Yield strength of steel
h Height of headed stud
h_b Height of I-beam bottom flange
h_c Depth of concrete slab
h_{ef} Effective embedment depth of stud
h_t Height of I-beam top flange
h_w Height of I-beam web
x Distance between concrete compression top tip fiber and neutral axis
Δ_{Fu} Elongation corresponding to F_u of headed stud
ψ_s Percentage elongation of I-beam after fracture
ψ_{st} Reduction in cross section of headed stud after fracture
δ_{max} Deflection of SCCB corresponding to P_{max}
δ_u Deflection of SCCB corresponding to P_u
δ_y Deflection of SCCB corresponding to P_y
ε_0 Peak strain at f_c of NWC
ε_F Fracture strain of steel
ε_u Ultimate strain of steel
ε_y Yielding strain of steel
κ Factor for $N_{u,P}$
σ-ε Stress versus strain

Acknowledgement

The authors would like to acknowledge the National Natural Science Foundation of China (Grant No. 51978459, 52178494, and 52278201) and Tianjin University (Grant no. 2019XRX-0026). The authors gratefully express their gratitude for the financial supports.

References

[1] Dalen K.V., "The strength of stud shear connectors at low temperatures", Canadian Journal of Civil Engineering, 10, 429-435, 1983.
[2] Long A.E., Dalen K.V., and Csagoly P., "The fatigue behavior of negative moment regions of continuous composite beams at low temperatures", Canadian Journal of Civil Engineering, 2, 98-115, 1975.
[3] Li X., Xia Z., Pu Q., and Yang Y., "Dynamical test and vehicle-bridge coupling analysis of Lasa River Bridge", Journal of Vibration and Shock, 26 (11), 129-132, 2007. (in Chinese)
[4] Yan J.B., Liu X.M., Liew J.Y.R., Qian X., and Zhang M.H., "Steel-concrete-steel sandwich system in Arctic offshore structures: materials, experiments, and design", Materials and Design, 91, 111-121, 2016.
[5] Yan J.B., Wang Z., and Wang X., "Behaviour of steel-concrete-steel sandwich plates under different ice-contact pressure", Advanced Steel Construction, 15 (1), 116-122, 2019.
[6] Stepanova N.A., "On the lowest temperatures on earth", Monthly Weather Reviewer, 6-10, 1958.
[7] Yan J.B., Xie J., and Ding K.R., "Stress relaxation behavior of prestressing strands under low temperatures", PCI Journal, 65 (1), 41-56, 2020.
[8] Elices M., Corres H., and Planas J., "Behaviour at cryogenic temperatures of steel for concrete reinforcement", ACI Journal Proceedings, 84 (3), 405-411, 1986.
[9] Dahmani L., Khenane A., Kaci S., "Behavior of the reinforced concrete at cryogenic temperatures", Cryogenics, 47, 517-525, 2007.
[10] Yan J.B., and Xie J., "Experimental studies on mechanical properties of steel reinforcements under cryogenic temperatures", Construction and Building Materials, 151, 661-672, 2017.
[11] Yan J.B., Liew J.Y.R., and Zhang M.H., "Mechanical properties of normal strength mild steel and high strength steel S690 in low temperature relevant to Arctic environment", Materials and Design, 61, 150-159, 2014.
[12] Yan J.B., Luo Y.L., Lin X.C., Luo Y.B., and Zhang L.X., "Effects of the Arctic low temperature on mechanical properties of Q690 and Q960 high-strength steels", Construction and Building Materials, 300 124022, 2021.
[13] Krstulovic-Opara N., "Liquefied natural gas storage: Material behavior of concrete at cryogenic temperatures", ACI Materials Journal, 104 (3), 297-306, 2007.
[14] Lee G.C., Shih T.S., and Chang K.C., "Mechanical properties of concrete at low temperature", Journal of Cold Regions Engineering, 2 (1) 13-24, 1988.
[15] Xie J., Li X.M., and Wu H.H., "Experimental study on the axial-compression performance of concrete at cryogenic temperatures", Construction and Building Materials 72, 380-388, 2014.
[16] MacLean T.J., and Lloyd A., "Compressive stress-strain response of concrete exposed to low temperatures", Journal of Cold Regions Engineering, 33 (4), 04019014, 2019.
[17] Yan J.B., Xie W.J., Zhang L.X., and Lin X.C., "Bond behaviour of concrete-filled steel tubes at the Arctic low temperatures", Construction and Building Materials, 210, 118-131, 2019.
[18] Montejo L.A., Sloan J.E., Kowalsky M.J., and Hassan T., "Cyclic response of reinforced concrete members at low temperatures", Journal of Cold Regions Engineering, 22, 79-102, 2008.
[19] Montejo L.A., Kowalsky M.J., and Hassan T., "Seismic behavior of flexural dominated reinforced concrete bridge columns at low temperatures", Journal of Cold Regions Engineering, 23 (1), 18-42, 2009.
[20] Montejo L.A., Kowalsky M.J., and Hassan T., "Seismic behavior of shear-dominated reinforced concrete columns at low temperatures", ACI Structural Journal, 106 (4), 445-454, 2009.
[21] Montejo L.A., Marx E., and Kowalsky M.J., "Seismic design of reinforced concrete bridge columns at subfreezing temperatures", ACI Structural Journal, 107 (4), 427-433, 2010.
[22] Mirzazadeh M.M., Noël M., and Green M.F., "Effects of low temperature on the static behaviour of reinforced concrete beams with temperature differentials", Construction and Building Materials, 112, 191-201, 2016.
[23] Mirzazadeh M.M., Noël M., and Green M.F., "Fatigue behavior of reinforced concrete beams with temperature differentials at room and low temperature", Journal of Structural Engineering, 143 (7), 04017056, 2017.
[24] El-Hacha R., Wight R.G., and Green M.F., "Prestressed carbon fiber reinforced polymer sheets for strengthening concrete beams at room and low temperatures", Journal of Composites for Construction, 8 (1) 3-13, 2004.
[25] Saiedi R., Fam A., and Green M.F., "Behavior of CFRP-prestressed concrete beams under high-cycle fatigue at low temperature", Journal of Composites Construction, 15 (4), 482-489, 2011.
[26] Bryan P.E., and Green M.F., "Low temperature behaviour of CFRP prestressed concrete beams", Canadian Journal of Civil Engineering, 23 464-470, 1996.
[27] Karbhari V.M., and Eckel D.A., "Effect of cold regions climate on composite jacketed concrete columns", Journal of Cold Regions Engineering, 8 (3), 73-86, 1994.
[28] Green M.F., Bisby L.A., Fam A.Z., and Kodur V.K.R., "FRP confined concrete columns: Behaviour under extreme conditions", Cement and Concrete Composites, 28, 928-937, 2006.
[29] Yan J.B., Dong X., and Zhu J.S., "Behaviours of stub steel tubular columns subjected to axial compression at low temperatures", Construction and Building Materials, 228, 116788, 2019.
[30] Yan J.B., Wang T., and Dong X., "Compressive behaviours of circular concrete-filled steel tubes exposed to low-temperature environment", Construction and Building Materials, 245, 118460, 2020.
[31] Yan J.B., Dong X., and Zhu J.S., "Compressive behaviours of CFST stub columns at low temperatures relevant to the Arctic environment", Construction and Building Materials, 223, 503-519, 2019.
[32] Yan J.B., Dong X., and Wang T., "Axial compressive behaviours of square CFST stub columns at low temperatures", Journal of Constructional Steel Research, 164, 105812, 2020.
[33] Yan J.B., Luo Y.L., Su L.F., Lin X.C., Luo Y.B., and Zhang L.X., "Low-temperature compression behaviour of square CFST columns using Q960 ultra-high strength steel", Journal of Constructional Steel Research, 183, 106727, 2021.
[34] Yan J.B., Zhang B., Feng J.Y., Du Y.S., Luo Y.B., and Shi Y.D., "Low-temperature compression behaviour of circular stub stainless-steel tubular columns", Advanced Steel Construction, 18 (3), 670-678, 2022.
[35] Yan J.B., Wang Z., and Xie J., "Compressive behaviours of double skin composite walls at low temperatures relevant to the arctic environment", Thin-Walled Structures, 140, 294-303, 2019.
[36] Yan J.B., Wang Z., and Wang T., "Compressive behaviours of steel-concrete-steel sandwich walls with J-hooks at low temperatures", Construction and Building Materials, 207, 108-121, 2019.
[37] Wang Z., Yan J.B., and Liu X.M., "Numerical and theoretical studies on double steel plate composite walls under compression at low temperatures", Advanced Steel Construction, 17 (4), 376-384, 2021.
[38] GB/T 50081-2019, Standard for test methods of concrete physical and mechanical properties, China Architecture and Building Press, Beijing, 2019 (in Chinese).
[39] GB/T 228.1-2010, Metallic materials-Tensile testing-Part 1: Methods of test at room temperature, China Standards Press, Beijing, China, 2010 (in Chinese).

[40] GB/T 228.3-2019, Metallic materials-Tensile testing-Part 3: Methods of test at low temperature, China Standards Press, Beijing, China, 2019 (in Chinese).
[41] Xie J., Zhu G.R., and Yan J.B., "Mechanical properties of headed studs at low temperatures in the Arctic infrastructures", Journal of Constructional Steel Research, 149, 130-140, 2018.
[42] GB 51081-2015, Technical code for application of concrete under cryogenic circumstance, China Planning Press, Beijing, China, 2015 (in Chinese).
[43] EN 1994-1-1: 2004, Eurocode 4, Design of composite steel and concrete structures-Part 1-1: General rules and rules for buildings, European Committee for Standardization, Brussels, Belgium, 2004.
[44] Yan, J.B., and Xie, J., "Shear behavior of headed stud connectors at low temperatures relevant to the Arctic environment", Journal of Structural Engineering, 144 (9), 04018139, 2018.
[45] Xie J., Kang E.C., Yan J.B., and Zhu G.R., "Pull-out behaviour of headed studs embedded in normal weight concrete at low temperatures", Construction and Building Materials, 264, 120692, 2020.